JOURNAL OF THE ATMOSPHERIC SCIENCES

Simple Spectral Models for Atmospheric Radiative Cooling

NADIR JEEVANJEE* AND STEPHAN FUEGLISTALER†

Princeton University, Princeton, New Jersey

ABSTRACT

Atmospheric radiative cooling is a fundamental aspect of the Earth's greenhouse effect, and is intrinsically connected to atmospheric motions. At the same time, basic aspects of longwave radiative cooling, such as its characteristic value of 2 K/day, its sharp decline (or 'kink') in the upper troposphere, and the large values of CO_2 cooling in the stratosphere, are difficult to understand intuitively or estimate with pencil-and-paper. Here we pursue such understanding by building simple spectral (rather than gray) models for clear-sky radiative cooling. We construct these models by combining the cooling-to-space approximation with simplified greenhouse gas spectroscopy and analytical expressions for optical depth, and we validate these simple models with line-by-line calculations.

We find that cooling rates can be expressed as a product of the Planck function, a vertical emissivity gradient, and a characteristic spectral width derived from our simplified spectroscopy. This expression allows for a pencil-and-paper estimate of the 2 K/day tropospheric cooling rate, as well as an explanation of enhanced CO_2 cooling rates in the stratosphere. We also use these models to attribute the upper tropospheric kink in radiative cooling to a decline in spectrally integrated transmissivity gradients.

1. Introduction

Atmospheric radiative cooling is a fundamental aspect of Earth's greenhouse effect, and is intrinsically connected to atmospheric motions. Although radiative equilibrium states with no atmospheric cooling are possible in principle, on Earth such states are unstable; this leads to a turbulent troposphere with deep convection in the tropics and baroclinic eddies in mid-latitudes, both of which lead to non-radiative-equilibrium temperature profiles which exhibit radiative cooling.

This tight coupling between radiative cooling, turbulence, and the hydrological cycle has many consequences. Perhaps foremost, radiative cooling characterizes the large-scale circulation, as the diabatic vertical velocity with which clear air subsides is given by $\omega_d = -\rho g \mathscr{H}_{net}/\Gamma$ (e.g. Mapes 2001, here $\mathscr{H}_{net}$ is clear-sky net radiative heating rate in K/day, positive for heating, and all other symbols have their usual meaning). This clear-sky subsidence velocity turns out to be remarkably uniform across the globe, because $\mathscr{H}$ is; indeed, a latitude-height distribution of the clear-sky, longwave only heating $\mathscr{H}$ (Figure 1a, taken from ECMWF reanalysis) shows that throughout most of the troposphere, $\mathscr{H} = -2 \pm 0.5$ K/day. (Inclusion of shortwave heating from water vapor results in a $\mathscr{H}_{net}$ of roughly -1 K/day, not shown.) Despite the robustness of this value, however, we cannot estimate $\mathscr{H}$ from first principles:[1] gray models are insufficient for this task (as discussed below), leaving only comprehensive radiative transfer schemes as a means for calculating $\mathscr{H}$.

Another consequence of the coupling between radiative cooling and turbulence is that wherever radiative cooling declines in the upper troposphere, latent heating by convection and baroclinic eddies must follow suit. To get a feel for this, we collapse the ECMWF cooling distribution in Fig. 1a onto a global radiative cooling profile by taking a meridional average (Fig. 1b, solid line). This profile has a characteristic value of -2 K/day through most of the troposphere, and also exhibits the well-known 'kink' around 200 hPa; this kink is significant, as it has been argued to constrain the altitude of clouds associated with both tropical convection (i.e. the FAT hypothesis, Hartmann and Larson 2002; Hartmann et al. 2001) as well as extratropical baroclinic eddies (Thompson et al. 2017).[2] Despite

*Corresponding author address: Nadir Jeevanjee, Geosciences Department, Princeton University, Princeton NJ 08544
E-mail: nadirj@princeton.edu

†Geosciences Department, Princeton University, Princeton NJ 08544

[1] Given the average outgoing longwave radiation (OLR) of 240 W/m^2 and a tropospheric mass of $\sim$ 8000 kg/m^2, one can estimate a global average $\mathscr{H}$ as $\mathscr{H} \approx -(240\ \text{W/m}^2)/(8 \times 10^3\ \text{kg/m}^2 \cdot 1000\ \text{J/kg/K}) = -2.5 \times 10^{-5}\ \text{K/s} = -2.5$ K/day. This calculation cannot tell us about the latitude-height distribution of $\mathscr{H}$, however, and moreover assumes that all OLR emanates from the atmosphere, an assumption which is reasonable in the global mean but does not hold locally (Costa and Shine 2012).

[2] For a recent critique of these arguments, however, see Seeley et al. (2019).

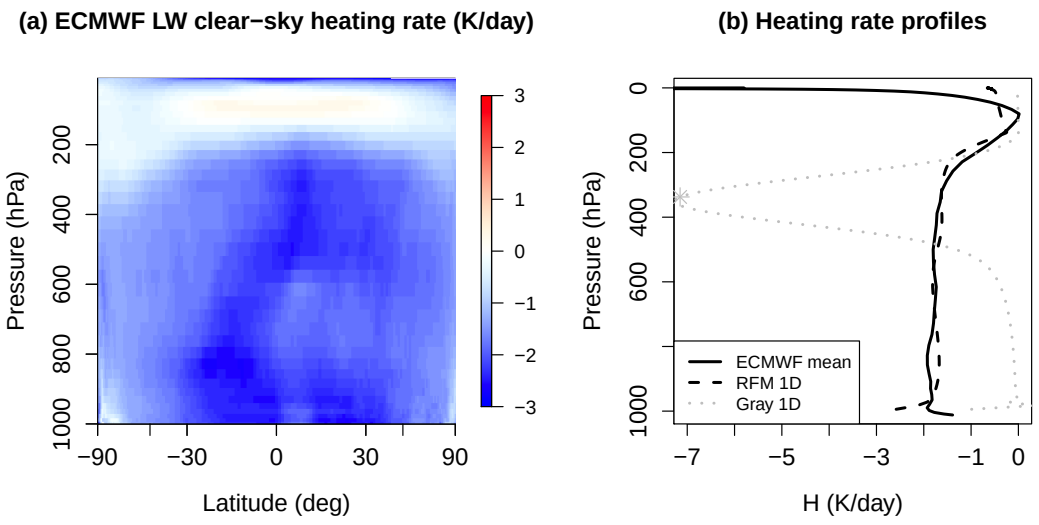

FIG. 1. **(a)** Zonal mean clear-sky longwave heating rates $\mathscr{H}$ from ECMWF reanalysis for June-July-August 2001. $\mathscr{H} = -2 \pm 0.5$ K/day across most of the troposphere. **(b)** Vertical heating rate profiles as calculated by globally averaging the ECMWF $\mathscr{H}$ (solid black line) and from our BASE atmosphere as calculated by RFM (dashed black line) and a gray model (solid gray line) tuned to have the same column-integrated cooling as RFM (i.e. same area under the curve). Gray star denotes the $\tau = 1$ level for the gray model. The 1D RFM calculation emulates the tropospheric ECMWF global mean, but the 1D gray model fails dramatically.

its importance, however, the kink has so far only been attributed qualitatively to a decline in 'water vapor emissivity', a notion which has not been made precise or quantified. Also, above the kink one sees $\mathscr{H}$ declining towards zero, but then rebounding sharply in the stratosphere. It is well known that this strong stratospheric cooling emanates from CO_2 molecules, not H_2O (e.g Zhu et al. 1992; Manabe et al. 1964), but we lack a simple explanation for how CO_2 cooling rates can be many times larger in the stratosphere than the troposphere, despite comparable temperature ranges in the two regions.

There are thus three basic questions we can ask about the $\mathscr{H}$ profile shown in Fig. 1b:

1. Why does it take on a characteristic value of - 2 K/day, and why is this value relatively robust across the troposphere?
2. What causes the kink around 200 hPa?
3. Why is CO_2 cooling enhanced in the stratosphere relative to the troposphere?[3]

The goal of this paper is to shed light on these questions. To do so, we will need to bridge the gap between the complex radiative transfer calculations used in Fig. 1 and intuitive gray models, which are still used in atmospheric modeling (see Section 8) but are *too* simple in the sense that they do not reproduce the phenomena of interest. To bring this into focus, we first emulate the ECMWF $\mathscr{H}$ profile in Fig. 1b with the $\mathscr{H}$ profile generated by an idealized, single-column calculation of radiative cooling from H_2O only in a constant lapse rate and constant relative humidity tropical atmosphere, using the line-by-line Reference Forward Model (RFM, dashed line of Fig. 1b; further details in Section 2a). This heavily idealized single column RFM calculation does a good job of emulating the tropospheric global average ECMWF profile. Despite the relative simplicity of this RFM calculation, however, it is still too complex to provide much understanding, as it still convolves intricate greenhouse gas spectroscopy with non-linear radiative transfer.

If we instead turn to a gray radiation model tuned to yield the same column-integrated cooling as the RFM profile,[4] we find instead that the gray model cannot emulate the RFM and ECMWF profiles: the gray radiative cooling profile has far too much vertical structure, and its upper-tropospheric heating rates err by a factor of three or more (Fig. 1b, gray line; see also Fig. S1 of Seeley et al. (2019)). There is thus indeed a gap between our simula-

[3] Note that the strong longwave stratospheric cooling rates are themselves fixed by the need to balance strong shortwave heating by ozone, so this question is really about how CO_2 exhibits such strong cooling in a stratosphere which is not significantly warmer than the troposphere.

[4] More precisely, we use the same thermodynamic profiles and absorber concentration as the RFM calculation, but use a non-pressure-broadened gray absorption coefficient tuned to yield the same column-integrated radiative cooling (of roughly 170 W/m^2) as the RFM calculation.

tion and understanding of radiative cooling, and answering the questions posed above will require bridging this gap.

To accomplish this we will consider spectral radiation, but will simplify greenhouse gas spectroscopy by approximating the spectrum of mass absorption coefficients $\kappa(k)$ of our greenhouse gases as piecewise exponentials, as also done in Wilson and Gea-Banacloche (2012). We will also simplify the radiative transfer using the cooling-to-space approximation (e.g. Jeevanjee and Fueglistaler 2019; Petty 2006; Green 1967; Rodgers and Walshaw 1966). These simplifications lead to a succession of simple spectral models, the SSM2D and SSM1D, constructed in Section 3. These models exhibit the phenomena of interest in questions 1-3 above but are analytically tractable, and are thus used to address those questions in Sections 4 – 7.

2. Preliminaries

Before building models of radiative cooling, we detail the line-by-line calculations which we use as a benchmark, and also review the qualitative picture of spectrally-resolved radiative cooling found in, e.g., Harries et al. (2008); Clough et al. (1992).

a. RFM calculations

All line-by-line calculations in this paper are performed with the Reference Forward Model (RFM, Dudhia 2017). We use HITRAN2016 spectroscopic data for the most common isotopologue of H_2O and CO_2 from 10–1500 $\text{cm}^{-1}$and 500-850 cm^{-1} respectively. For our BASE case we consider an idealized atmosphere with H_2O as the only greenhouse gas, surface temperature $T_s = 300$ K, a constant lapse rate of $\Gamma = 7$ K/km up to to an isothermal stratosphere at $T_{\text{strat}} = 200$ K, and a vertically uniform relative humidity of RH=0.75. We run RFM at a spectral resolution of 0.1 cm^{-1} and a uniform vertical resolution of 100 m up to model top at 50 km. We output optical depth, fluxes, heating rates, and absorption coefficients, all as a function of wavenumber and height. For simplicity in comparing to our analytical model below, RFM optical depth is calculated along a vertical path (zenith angle of zero), and fluxes and heating rates are computed using a two-stream approximation (rather than RFM's default four-stream) with a diffusivity factor of $D = 1.5$ [as specified in Dudhia (2017), following Clough et al. (1992)].[5] In BASE we omit the water vapor continuum (Shine et al. 2012), not because it is negligible but simply for analytic tractability. The effects of the water vapor continuum, as parameterized in RFM (using the MT_CKD continuum, Mlawer et al. 2012) are considered in Appendix A.

[5]For reproducibility, note also that we run RFM with the BFX flag disabled. This means the Planck function $B(k,T)$ is assumed constant within an RFM vertical grid cell, rather than assuming a sub-grid vertical variation of the Planck function which is linear in height. Here k denotes wavenumber.

b. The shape of $\mathscr{H}_k$

The object of interest in this paper is the clear-sky longwave radiative heating $\mathscr{H}$. But, $\mathscr{H}$ is simply the spectral integral of the spectrally-resolved heating

$$\mathscr{H}_k \equiv \frac{g}{C_p}\partial_p F_k \quad (\text{K/s/cm}^{-1}) \tag{1}$$

where F_k is spectrally-resolved net upward LW flux in $\text{W/m}^2/\text{cm}^{-1}$. Thus, any understanding of $\mathscr{H}$ must stem from an understanding of $\mathscr{H}_k$, and in the next section we will indeed begin by building a simple quantitative model for $\mathscr{H}_k$. In the meantime, however, it will be useful to review the qualitative physics of $\mathscr{H}_k$, following e.g. Harries et al. (2008); Clough et al. (1992).

Figure 2c shows $\mathscr{H}_k$ from BASE as computed by RFM. There is a strong band of cooling for $k < 800$ cm^{-1}, and a weaker band for $k > 1200$ cm^{-1}. To understand these structures, we consider the optical depth τ_k, measured from $p = 0$ and given by

$$\tau_k(p) \equiv \int_0^p \underbrace{\kappa(k,T,p')}_{\text{m}^2/\text{kg}} \underbrace{q_v \frac{dp'}{g}}_{\text{kg/m}^2} . \tag{2}$$

Here q_v is water vapor specific humidity (kg/kg) and the mass absorption coefficient κ (kg/m^2) depends not only on wavenumber k but also on T and p, due to temperature-scaling and pressure broadening (Pierrehumbert 2010). All other symbols have their usual meaning. Note that since κ is an effective area per unit mass, and since the rest of the integrand in (2) is just the mass per unit area of absorber above level p (i.e. the path length), τ_k can be interpreted as the effective area of absorbers above level p per unit geometric area.

The spectral distribution of optical depth as output from RFM is shown in Fig. 2b, which also plots the $\tau_k = 1$ levels for each k. The two diagonal bands in the $\mathscr{H}_k$ plot correspond to two diagonal $\tau_k = 1$ bands, which is where we expect emission to space at a given k to maximize [Jeevanjee and Fueglistaler (2019); Wallace and Hobbs (2006); Petty (2006); see also Fig. 1b, and Section 2c below]. The shape of these $\tau_k = 1$ bands in the $k-p$ plane can themselves be understood in terms of reference absorption coefficients

$$\kappa_{\text{ref}}(k) \equiv \kappa(k, T_{\text{ref}}, p_{\text{ref}}) \tag{3}$$

where we take $(T_{\text{ref}}, p_{\text{ref}}) = (300\text{ K}, 1\text{ atm})$. These coefficients, also output from RFM, are shown in Fig. 2a. The two $\tau_k = 1$ bands in Fig. 2b correspond to the two absorption bands evident in the κ_{ref} plot: the pure rotation band ($k < 1000$ cm^{-1}), and the vibration-rotation band ($1000 < k < 1450$ cm^{-1}). By (2), where κ_{ref} is relatively large then $\tau_k = 1$ occurs at relatively high altitudes, and vice-versa, so that plots of κ_{ref} and $\tau_k = 1$ levels must necessarily have the same shape. This shape also manifests in

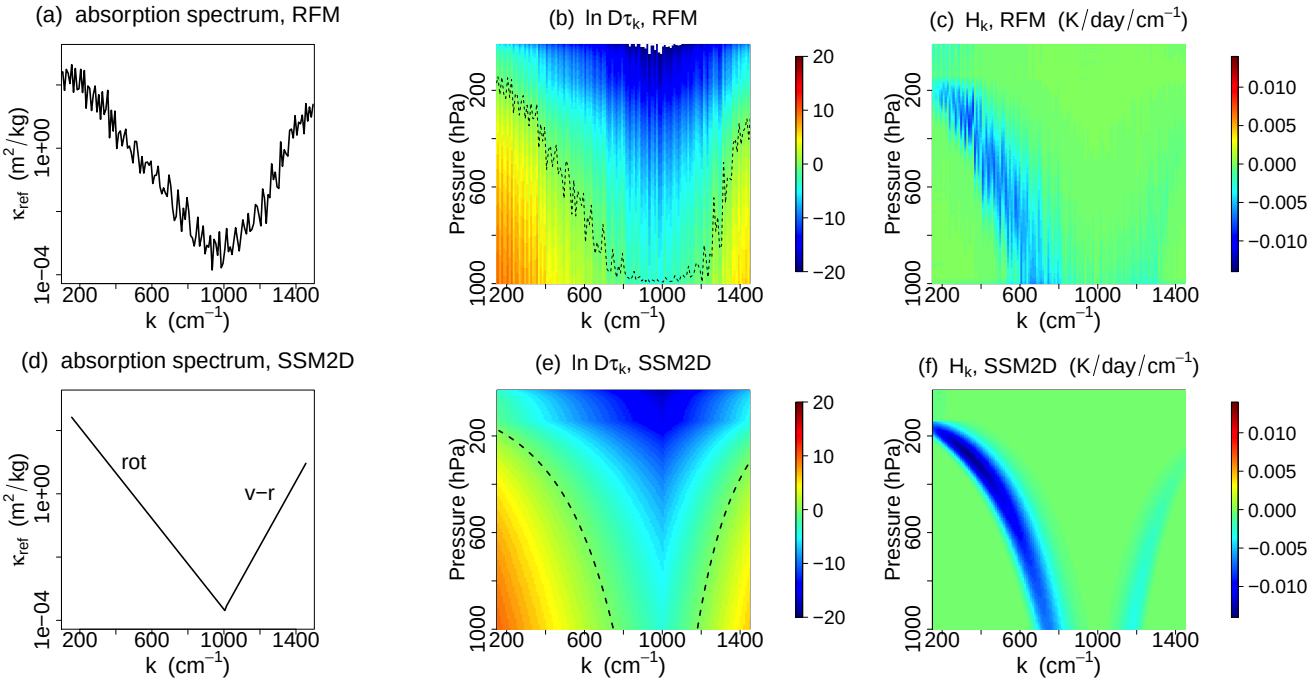

FIG. 2. Comparison between RFM output and the SSM2D, as follows: **(a,d)** H_2O absorption spectrum $\kappa_{\rm ref}$, at $(T_{\rm ref}, p_{\rm ref})$ = (300 K, 1 atm) from RFM and our linear fit (9), respectively **(b,e)** Logarithm of diffusion parameter D times optical depth τ_k, from RFM and Eqn. (10), respectively, along with $\tau_k = 1$ contours. **(c,f)** Spectrally resolved heating $\mathscr{H}_k$, from RFM and the SSM2D [Eqns. (4) and (10)]. All plots show averages over 10 cm^{-1} bins, with log averaging in (a) and linear averaging in (b) and (c). These panels show that the spectrally resolved cooling $\mathscr{H}_k$ can be understood as emission from $\tau_k = 1$ levels, where the height of these levels is determined by $\kappa_{\rm ref}(k)$, and that the SSM2D captures this physics.

the $\mathscr{H}_k$ field. These multiple manifestations of H_2O spectroscopy can all be seen in the top row of Fig. 2.

c. *The cooling-to-space approximation and the transmissivity gradient*

Strictly speaking, the $\tau = 1$ law invoked above applies only to the emission of OLR (or 'cooling-to-space'), not radiative heating rates *per se*. This is because the latter includes not just cooling-to-space, but also radiative exchange between atmospheric layers as well as the surface (Green 1967). However, these 'exchange terms' are often negligible (Jeevanjee and Fueglistaler 2019; Clough et al. 1992; Rodgers and Walshaw 1966), so radiative cooling may indeed be approximated solely by the cooling-to-space term. This yields the *cooling-to-space approximation*

$$\partial_p F_k \;\approx\; \pi B(k,T)\frac{\partial \mathscr{T}_k}{\partial p}\;. \tag{4}$$

Here $\mathscr{T}_k \equiv \exp(-\tau_k)$ is the transmission function and $\pi B(k,T)\frac{\partial \mathscr{T}_k}{\partial p}$ is the cooling-to-space (or CTS) term in pressure coordinates. This is the differential contribution of an atmospheric layer to the OLR at wavenumber k, and is given by Planck emission $\pi B(k,T)$ times the transmissivity gradient $\partial_p \mathscr{T}_k$.

How should one think about and evaluate the transmissivity gradient in (4)? For this purpose it is convenient to define the optical depth exponent β,

$$\beta \;\equiv\; \frac{\partial \ln \tau_k}{\partial \ln p}\;. \tag{5}$$

We will see below that β is constant for CO_2, and roughly constant for H_2O. We can use β to write the transmissivity gradient as

$$\frac{\partial \mathscr{T}_k}{\partial p} \;=\; -\frac{\beta}{p}\tau_k e^{-\tau_k}\;. \tag{6}$$

The factor $\beta/p = \partial_p \ln \tau_k$ is an inverse 'scale pressure' for optical depth, and measures the rate at which τ_k increases by one e-folding. The other factor $\tau_k e^{-\tau_k}$ is a kind of 'weighting function' which peaks at $\tau_k = 1$, thus giving rise to the $\tau = 1$ law. [Strictly speaking one also needs to worry about vertical variations in $1/p$ as well as the Planck function, but these turn out to be secondary, Jeevanjee and Fueglistaler (2019).] Thus, the peak magnitude of (6) can be estimated by evaluation at $\tau_k = 1$:

$$\left.\frac{\partial \mathscr{T}_k}{\partial p}\right|_{\tau_k=1} \;=\; -\,\frac{1}{e}\frac{\beta}{p}\;. \tag{7}$$

We thus have the key result that β/p governs the peak magnitude of the transmissivity gradient. As such, this quantity will appear frequently throughout this paper.[6] In particular, the variations in β/p between CO_2 and H_2O, and between troposphere and stratosphere, will play a significant role in answering question 3 in Section 7.

As a caveat, note that even though the CTS approximation and the accompanying $\tau = 1$ law appear to hold quite well for Earth's atmosphere, these rules are not entirely general. The CTS approximation fails in pure gray radiative equilibrium (which has zero radiative cooling everywhere), and turns out to also depend on the choice of vertical coordinate. These issues, as well as criteria for the CTS approximation (and the $\tau = 1$ law) to hold, are the subject of the companion paper Jeevanjee and Fueglistaler (2019).

3. Simple spectral models for H_2O cooling

a. SSM2D: a model for spectrally-resolved cooling $\mathscr{H}_k$

We begin by building a simple model for spectrally and vertically resolved heating rates $\mathscr{H}_k$, focusing for the moment on H_2O. Since the model has two resolved dimensions (k and p), we will refer to it as our two-dimensional simple spectral model (SSM2D).

The first step in building the SSM2D for H_2O is to simplify H_2O spectroscopy, i.e. the functional form of H_2O mass absorption coefficients $\kappa_{\text{ref}}(k)$ (Fig. 2a). We do this by following Wilson and Gea-Banacloche (2012) and first coarse-graining $\ln \kappa_{\text{ref}}(k)$ over spectral intervals of 10 cm^{-1} (note that this is already what is plotted in Fig. 2a). We then delineate the H_2O rotation band (**rot**) and vibration-rotation band (**v-r**) as

$$\begin{aligned} &\textbf{rot}: \quad k_{\text{rot}} \equiv 150 < k < 1000 \text{ cm}^{-1} \\ &\textbf{v-r}: \quad 1000 < k < 1450 \text{ cm}^{-1} \equiv k_{\text{v-r}} . \end{aligned} \tag{8}$$

We then apply a linear fit to $\ln \kappa_{\text{ref}}(k)$ within each band to obtain a piecewise exponential approximation for $\kappa_{\text{ref}}(k)$:

$$\kappa_{H_2O}(k) \equiv \begin{cases} \kappa_{\text{rot}} \exp\left(-\frac{k-k_{\text{rot}}}{l_{\text{rot}}}\right) & \text{for } k \text{ in } \textbf{rot} \\ \kappa_{\text{v-r}} \exp\left(-\frac{k_{\text{v-r}}-k}{l_{\text{vr}}}\right) & \text{for } k \text{ in } \textbf{v-r}. \end{cases} \tag{9}$$

The parameters $\ln \kappa_{\text{rot}}$ and $\ln \kappa_{\text{v-r}}$ are obtained as the maxima of the corresponding straight line fits, and l_{rot} and l_{vr} as the corresponding slopes. These parameter values are tabulated in Table 1, which also includes other symbol definitions. The l parameters have units of cm^{-1}, and describe how fast κ_{ref} exponentially declines with k. These parameters, and their analogs for CO_2, will play a crucial role in what follows.

[6] This is one reason why we choose to write (6) in its particular form, with a mix of p and τ_k coordinates. Another reason is that the form (6) is amenable to the analytical spectral integration we perform in Section 3b.

With the simplified absorption spectra (9) in hand we can now construct simplified expressions for H_2O optical depth τ_k. This is done using the analytical expression for water vapor path from SI eqn. 2 of Koll and Cronin (2018), except we consider an unsaturated atmosphere, replace the T factor out front with an average tropospheric temperature $T_{\text{av}} = (T_s + T_{\text{strat}})/2$ (results are not sensitive to this approximation), and consider an arbitrary lapse rate Γ. Combining this expression for water vapor path with an approximate pressure-broadening factor p/p_{ref} yields

$$\tau_k = \kappa_{H_2O}(k) \frac{p}{p_{\text{ref}}} \text{WVP}_0 \exp\left(-\frac{L}{R_v T}\right) . \tag{10}$$

Here $\text{WVP}_0 \exp(-L/R_v T)$ is the water vapor path (kg/m^2), where WVP_0 is a constant given by

$$\text{WVP}_0 \equiv D \frac{T_{\text{av}} \text{RH} p_v^\infty}{\Gamma L} . \tag{11}$$

Here D is our diffusivity factor of 1.5 and $p_v^\infty = 2.5 \times 10^{11}$ Pa is a reference value for the saturation vapor pressure p_v^*, satisfying $p_v^*(T) = p_v^\infty \exp(-L/R_v T)$.

Substituting (10) into the CTS approximation (4) then yields an approximation for $\mathscr{H}_k$. This $\mathscr{H}_k$, along with the fitted κ_{H_2O} of (9) and optical depth τ_k of (10), constitute the SSM2D. These fields are shown in the bottom row of Fig. 2, directly underneath their RFM counterparts. For all three fields the SSM2D captures the gross behavior of the RFM calculation.

At the same time, of course, the SSM2D neglects all fine-scale spectral structure. One drawback of this is that the SSM2D overestimates the peak values of $\mathscr{H}_k$ (Fig. 2c,f). This occurs because the fine-scale structure in the RFM calculation, when combined with a coarse-graining into 10 cm^{-1} bins as we have done here, yields a $\mathscr{H}_k$ field which is 'smeared out' in the $k-p$ plane, such that the cooling around a given (k,p) occurs over a larger (k,p) range in RFM than in the SSM2D, and must thus have a smaller magnitude in RFM.

Upon spectral integration, however, such errors cancel, and the SSM2D will produce reasonable values for the spectrally integrated cooling $\mathscr{H}$, as we will see below. Given this, the SSM2D could be used at this point to try and answer questions 1-3 posed above. However, further insight can be gained by making additional approximations and analytically integrating the $\mathscr{H}_k$ field over wavenumber space. We turn to this next.

b. SSM1D: a model for spectrally-integrated cooling $\mathscr{H}$

We now construct a 1D simple spectral model (SSM1D) for spectrally integrated cooling $\mathscr{H}$. Our starting point will be the SSM2D for $\mathscr{H}_k$, which itself is still too complicated to be analytically integrated over wavenumber space, so further approximations will be required. (The SSM1D will thus *not* be equivalent to simply integrating

Quantity	Symbol	Units
Wavenumber	k	cm^{-1}
Mass absorption cofficient (with T, p dependence)	κ	m^2/kg
Reference mass absorption cofficients (at T= 300 K, p = 1000 hPa)	κ_{ref}, $\kappa_{\mathrm{H_2O}}$, $\kappa_{\mathrm{CO_2}}$	m^2/kg
Optical depth at wavenumber k	τ_k	dimensionless
Transmissivity at wavenumber k	$\mathscr{T}_k \equiv \exp(-\tau_k)$	dimensionless
Optical depth exponent	$\beta \equiv \frac{d\ln\tau_k}{d\ln p}$	dimensionless
Planck function at wavenumber k, temperature T	$B(k,T)$	$\mathrm{W/m^2/sr/cm^{-1}}$
Clear-sky longwave heating rate	$\mathscr{H}$	K/day
Spectrally resolved clear-sky longwave heating rate	$\mathscr{H}_k$	$\mathrm{K/day/cm^{-1}}$
Diffusion coefficient for two-stream approximation	D	dimensionless
Reference water vapor path	$\mathrm{WVP_0}$	$\mathrm{kg/m^2}$
Spectroscopic band	j, denotes **rot**, **v-r**, or Q	—
$\tau_k = 1$ wavenumber profile in band j	$k_{1,j}(\mathrm{p})$	cm^{-1}
Heating rate integrated over band j	$\mathscr{H}_j$	K/day
Effective emitting width	Δk	cm^{-1}
Spectrally integrated transmissivity gradient	$\overline{\partial_p \mathscr{T}_k}$	$\mathrm{cm^{-1}/hPa}$
SSM spectroscopy parameters	$\mathrm{H_2O}$	$\mathrm{CO_2}$
Wavenumbers at band maxima	$k_{\mathrm{rot}} = 150\ \mathrm{cm}^{-1}$ $k_{\text{v-r}} = 1450\ \mathrm{cm}^{-1}$	$k_Q = 667.5\ \mathrm{cm}^{-1}$
Band-maximum reference absorption coefficients	$\kappa_{\mathrm{rot}} = 260\ \mathrm{m}^2/\mathrm{kg}$ $\kappa_{\text{v-r}} = 10\ \mathrm{m}^2/\mathrm{kg}$	$\kappa_Q = 165\ \mathrm{m}^2/\mathrm{kg}$
Spectroscopic decay parameter	$l_{\mathrm{rot}} = 60\ \mathrm{cm}^{-1}$ $l_{\mathrm{vr}} = 42\ \mathrm{cm}^{-1}$	$l_Q = 13\ \mathrm{cm}^{-1}$

TABLE 1. (Top) Definition of important symbols used throughout the paper. (Bottom) Spectroscopic parameters used in the SSM2D and SSM1D. The k_{rot} and $k_{\text{v-r}}$ are chosen by inspection of Fig. 2a, and k_Q is chosen to be proximate to the central 667.66 cm^{-1} Q branch line. The κ and l parameters, on the other hand, are not externally specified but result from fits to RFM output. See text for details.

the SSM2D numerically over wavenumber space, though we will employ this latter quantity later on as well.) To proceed we need two more derived quantities. The first is an expression for β for $\mathrm{H_2O}$, which we obtain by substituting our expression (10) for τ_k into the definition (5) of β:

$$\beta_{\mathrm{H_2O}} \;=\; 1 + \frac{L}{R_v T}\frac{\Gamma R_d}{g}\;. \tag{12}$$

Typical tropospheric values[7] for $\Gamma = 7$ K/km are $\beta_{\mathrm{H_2O}} = 5.5 \pm 1$.

The second (and more important) derived quantity is the wavenumber profile $k_{1,j}(p)$, which parameterizes the $\tau_k = 1$ contour in the $k-p$ plane for band j and hence gives the corresponding locus of cooling in the $k-p$ plane (here j denotes either the **rot** or **v-r** bands from (8)). We obtain analytical expressions for $k_{1,j}$ by substituting $\kappa_{\mathrm{H_2O}}$ from Eqn. (9) into the τ_k formula Eqn. (10), setting $\tau_k = 1$, and solving for k in each band, yielding

$$\begin{aligned} k_{1,\mathrm{rot}} &= k_{\mathrm{rot}} + l_{\mathrm{rot}}\left[\ln(\kappa_{\mathrm{rot}}\mathrm{WVP_0}) + \ln(p/p_{\mathrm{ref}}) - \frac{L}{R_v T}\right] \\ k_{1,\text{v-r}} &= k_{\text{v-r}} \;-\; l_{\mathrm{vr}}\left[\ln(\kappa_{\text{v-r}}\mathrm{WVP_0}) + \ln(p/p_{\mathrm{ref}}) - \frac{L}{R_v T}\right]. \end{aligned} \tag{13}$$

These $\tau = 1$ contours are overlaid over the simple τ_k distribution in Fig. 2e, and capture the overall shape and x and y intercepts of the noisier $\tau = 1$ contours diagnosed from RFM output (Fig. 2b). Note that the exponentials in $\kappa_{\mathrm{H_2O}}(k)$ and $\exp(-L/R_v T)$ cancel out in (13), leaving $k_{1,j}$ with a strong dependence on T and only a logarithmic dependence on other variables, which will be of significance in Section 5.

With these ingredients in place we now obtain an analytical approximation for the spectrally integrated heating in band j, denoted $\mathscr{H}_j$. We begin by integrating (1) over band j at a given p, assuming the limits of the spectral integral are implicitly given by the appropriate wavenumber range from (8). We also invoke the CTS approximation (4) as well as Eqn. (6). This yields

$$\mathscr{H}_j \;=\; -\frac{g}{C_p}\frac{\beta}{p}\int dk\, \pi B(k,T)\,\tau_k \exp(-\tau_k)\;. \tag{14}$$

To evaluate this integral, recall that the function $\tau_k \exp(-\tau_k)$ peaks at $\tau_k = 1$ (with corresponding k value $k_{1,j}$), and that its integral $\int_0^\infty d\tau_k\, \tau_k \exp(-\tau_k) = 1$. These properties are shared by the Dirac delta function $\delta(\tau_k - 1)$, so we might approximate $\tau_k \exp(-\tau_k)$ by $\delta(\tau_k - 1)$. This approximation can be applied to (14) once we convert $\delta(\tau_k - 1)$ to a delta function in k-coordinates, using the appropriate chain rule (e.g. Gasiorowicz 2003) as well as

[7] In the tropics, where Γ is set by the moist adiabat and is roughly 4 K/km near the surface and 9 K/km in the upper troposphere, the variation in β is larger: $\beta_{\mathrm{H_2O}} \approx 5.5 \pm 2$.

Eqns. (10) and (9):

$$\delta(\tau_k - 1) \;=\; \left|\frac{\partial \tau_k}{\partial k}(k_{1,j})\right|^{-1} \delta(k - k_{1,j}) \;=\; l_j\, \delta(k - k_{1,j})\;.$$

Note the appearance of the l_j parameter here, which we comment on further below. Plugging this last equation into (14) and performing the now trivial spectral integration yields finally our desired approximation expression for band-wise integrated radiative cooling,

$$\mathscr{H}_j \;\approx\; -\frac{g}{C_p}\pi B(k_{1,j},T)\frac{\beta}{p}l_j\;. \tag{15}$$

Note that $B(k_{1,j},T)$ gives the Planck emission as a function of height *only,* since $k_{1,j}$ [cf. (13)] is a function of height which gives the wavenumber which cools-to-space at a given height . Equation (15), along with its inputs (12) and (13), constitute the SSM1D.

4. Interpretation and estimation

a. Interpretation

The SSM1D (15) is a central result of this paper. How should we interpret it? From (7) we know that the β/p factor in (15) is closely related to the transmissivity gradient $\partial_p \mathscr{T}_k$ evaluated at $\tau_k = 1$. Furthermore, $-\partial_p \mathscr{T}_k$ can be interpreted as the 'emissivity-to-space' gradient: for an atmospheric layer of thickness Δp we can interpret $-\Delta p \partial_p \mathscr{T}_k = \Delta p (d\tau_k/dp)\mathscr{T}_k$ as its 'emissivity to space', since $\Delta p(d\tau_k/dp)$ gives the absolute emissivity of the layer and $\mathscr{T}_k$ is the fraction of emitted radiation that escapes to space. Thus $-\partial_p \mathscr{T}_k$ is the emissivity-to-space gradient (in pressure coordinates). This suggests that we re-write (15) as

$$\mathscr{H}_j \;=\; -\frac{g}{C_p}\underbrace{\pi B(k_{1,j},T)}_{\substack{\text{Planck}\\ \text{emission}\\ (\mathrm{W/m^2/cm^{-1}})}}\underbrace{\left(\frac{1}{e}\frac{\beta}{p}\right)}_{\substack{\text{emissivity}\\ \text{gradient}\\ (1/\mathrm{Pa})}}\underbrace{(l_j e)}_{\substack{\text{spectral}\\ \text{width } \Delta k\\ (\mathrm{cm^{-1}})}}\;. \tag{16}$$

The factor $l_j e$ in (16) can be interpreted as an 'effective emitting width' Δk, i.e. as the width of the spectral region at any given height that is cooling to space. For the H_2O **rot** band we find $\Delta k = l_{\mathrm{rot}} e \approx 165\ \mathrm{cm^{-1}}$, in rough eyeball agreement with the width of the active cooling regions in Fig. 2c,f. That l_j simultaneously gives the inverse decay rate of $\kappa(k)$ [Eqn. (9)] as well as the effective emitting width Δk may seem mysterious first, but is consistent in that a larger decay rate for $\kappa(k)$ implies a narrower peak of $\tau_k e^{-\tau_k}$ in k-coordinates in (14), and hence a smaller Δk.

In summary, then, Eqn. (16) says that radiative heating at a given height may be interpreted as spectral Planck emission, times a spectral width, times an appropriate measure of emissivity, all evaluated at $k_{1,j}$ where $\tau_{k_{1,j}} = 1$. This yields a flux divergence (which in pressure coordinates has units $\mathrm{W/m^2/Pa}$), which can be multiplied by g/C_p to get a heating rate in K/day.

b. A back-of-the-envelope estimate of $\mathscr{H}$

A primary motivation for developing the SSM1D is to address question 1 from the introduction and make a back-of-the-envelope estimate of $\mathscr{H}$, which we now do. We first take a mid-tropospheric $(T,p) = (260\ \mathrm{K}, 500\ \mathrm{hPa})$, which corresponds to $k_{1,\mathrm{rot}} = 500\ \mathrm{cm^{-1}}$ and $k_{1,\text{v-r}} = 1350\ \mathrm{cm^{-1}}$, and evaluate $\pi B(k_{1,j},T)$:

$$\begin{aligned}\pi B(k_{1,\mathrm{rot}}, 260\ \mathrm{K}) &\approx 0.3\ \mathrm{W/m^2/cm^{-1}}\\ \pi B(k_{1,\text{v-r}}, 260\ \mathrm{K}) &\approx 0.05\ \mathrm{W/m^2/cm^{-1}}\;.\end{aligned}$$

Thus **v-r** Planck emission is roughly 1/6 of that for **rot**, which explains why the cooling in the **v-r** band in Fig. 2c,f is much smaller than that in the **rot** band. We thus neglect $\mathscr{H}_{\textbf{v-r}}$ for this estimate, and also take $\beta_{H_2O} \approx 5$. We then have

$$\begin{aligned}\mathscr{H} &\approx -\frac{g}{C_p}\pi B(k_{1,\mathrm{rot}},T)\, l_{\mathrm{rot}}\frac{\beta_{H_2O}}{p}\\ &\approx -\left(10^{-4}\frac{\mathrm{K/s}}{\mathrm{W/m^2/hPa}}\right)(20\ \mathrm{W/m^2})\left(\frac{1}{100\ \mathrm{hPa}}\right)\\ &= -2\times 10^{-5}\ \mathrm{K/s}\\ &\approx -2\ \mathrm{K/day}\;.\end{aligned} \tag{17}$$

Thus the SSM1D indeed allows us to quickly estimate the characteristic value $\mathscr{H} \approx -2$ K/day, using only fundamental constants, the atmospheric lapse rate (used in β), a typical value of the Planck function, and the RFM-derived parameter l_{rot}, which characterizes water vapor spectroscopy.

5. Validation and parameter sensitivities

We now seek to evaluate the SSM2D and SSM1D $\mathscr{H}$ profiles against the RFM benchmark, as well as gain insight into why the -2 K/day value seems relatively robust across the troposphere (Fig. 1a and question 1 above). To this end, Figure 3 shows $\mathscr{H}_{\textbf{rot}} + \mathscr{H}_{\textbf{v-r}}$ as calculated via RFM, SSM2D, and SSM1D. The SSM profiles (1D and 2D) track each other closely but underestimate cooling near the surface, an error due to the CTS approximation (Jeevanjee and Fueglistaler 2019). The SSM profiles also overestimate cooling in the upper atmosphere and underestimate cooling in the stratosphere, another drawback of our simplified spectroscopy (9) which doesn't account for the strongly absorbing wavenumbers near the center of spectral lines deep in the rotation band ($k < 300\mathrm{cm^{-1}}$ or so), which emit from the stratosphere rather than the troposphere. Despite these errors and approximations, however, the tropospheric SSM profiles lie in the characteristic

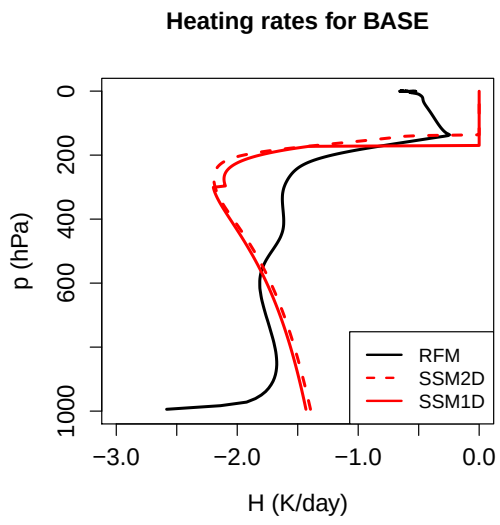

FIG. 3. Heating rate profiles calculated for our BASE case, using RMF, the SSM2D, and the SSM1D. Despite errors, the SSM2D and SSM1D capture the characteristic -2 ± 0.5 K/day magnitude of $\mathscr{H}$ from water vapor. See text for further discussion. Note that the water vapor continuum is turned off in the RFM BASE run.

$\sim 2 \pm 0.5$ K/day range produced by comprehensive radiation calculations. The SSM profiles also both seem to reproduce the upper tropospheric kink, which was the subject of question 2 above, and to which we return in Section 6 below.

To further test the SSM1D, as well as understand the sensitivity of $\mathscr{H}$ to humidity and temperature variations, we perturb our atmospheric column. In one perturbation calculation we change RH from 0.75 to 0.3, and in another we change the lapse rate Γ from 7 to 5 K/km. We run RFM and also evaluate the SSM1D on these two perturbed atmospheres, with the results shown in Figs. 4a,b (we cut-off the RFM profiles at the same height that the SSM1D profiles go to zero, for clarity). Both the RFM and simple model profiles show a marked insensitivity to RH. Both models also show a reduction in cooling in the middle and lower troposphere of roughly 30% with the reduction in Γ (in the upper troposphere this signal becomes convolved with that from the differing upper-tropospheric temperatures). These relatively small sensitivities, which are consistent with the relative uniformity of clear-sky $\mathscr{H}$ across the globe (Fig. 1), can be understood using Eqns. (15) as well as (13). These show that the change in RH only affects $k_{1,j}$, decreasing WVP_0 by roughly a factor of two and hence changing the $k_{1,j}$ by only $l_j \ln 2 \approx 35$ cm^{-1}, not enough to significantly change the Planck emission $B(k_{1,j},T)$. Changing Γ yields similarly small changes in $k_{1,j}$ but also has the additional effect of decreasing β; this is not negligible but is still a small change of roughly 30% (cf. Eqn. (12)), leading to a similar reduction in $\mathscr{H}$ (physically, reducing the vertical temperature gradient lowers water vapor emissivity gradients because of Clausius-Clapeyron, which lowers the flux divergence per unit pressure and hence the heating rate). Taken together, then, neither these RH or Γ variations (which are typical of such variations across the globe) significantly change the characteristic value of $\mathscr{H}$, because they are unable to significantly change Planck emission or vertical emissivity gradients (as encapsulated in β). This provides some insight into question 1 above. At the same time, of course, these perturbations are highly idealized, a point we return to in Section 8.

The final parameter to vary is T_s, which we vary across $T_\mathrm{s} = (270, 280, 290, 300)$ K, leaving RH and Γ unchanged from BASE. The comparison of $\mathscr{H}$ for these atmospheres is shown in Figs. 4c,d. The RFM and the SSM1D $\mathscr{H}$ profiles behave similarly, with both weakening from roughly -2 K/day to roughly -1 K/day at $T_\mathrm{s} = 270$ K. To the extent that the SSM1D captures this for the right reasons, Eqn. (15) tells us that this must be due to a weakening Planck function (which, at fixed p, is being evaluated at both lower k and lower T as T_s decreases). Both the RFM and SSM1D profiles also decrease in vertical extent with decreasing T_s, due to shoaling of the troposphere. These behaviors are also evident in the ECMWF $\mathscr{H}$ distribution in Fig. 1a, particularly in the southern (winter) hemisphere.

The foregoing explains to some degree the magnitude of latitudinal variations in $\mathscr{H}$, but does not explain the vertical uniformity of $\mathscr{H}$ profiles evident in Fig. 1. Some insight into this can also be gained from the SSM1D (15), which tells us that this uniformity is largely coincidental, and arises from a cancellation between increasing transmissivity gradients (as encapsulated in β/p) and a declining Planck function $\pi B(k_{1,j},T)$. This suggests there is no fundamental constraint that $\mathscr{H}$ be uniform in the vertical, and indeed the SSM1D profile in Fig. 3 is noticeably less uniform than RFM. Furthermore, even simply changing the lapse rate Γ is sufficient to make $\mathscr{H}$ notably less uniform, in both RFM and the SSM1D (Fig. 4).

At the same time, all of these profiles are much more vertically uniform than that due to a grey model (Fig. 1b); this is simply because a gray model can only reach $\tau = 1$ at one height, around which cooling will be concentrated, whereas real greenhouse gas spectroscopy yields a distribution of $\tau = 1$ heights (Fig. 2), and hence more uniformly distributed cooling.

6. The upper-tropospheric kink

We now turn to question 2 above, about the origin of the upper tropospheric kink in $\mathscr{H}$. By Eqn. (4), the two places to look for an explanation are the Planck function $B(k,T)$

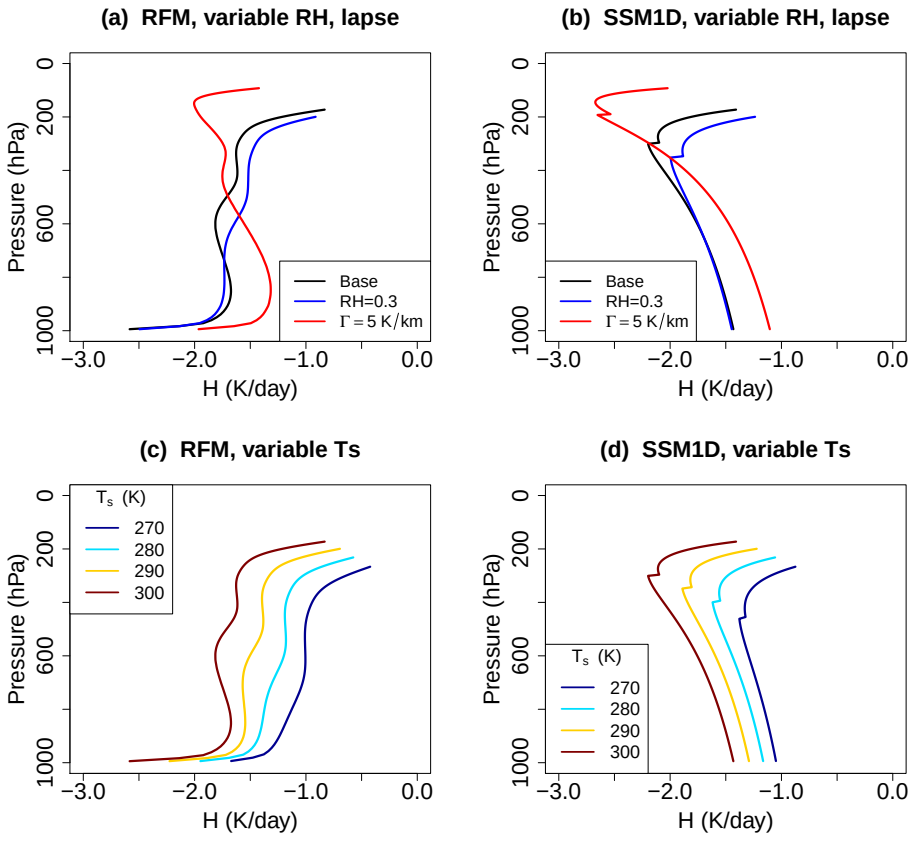

FIG. 4. **(a)** Profiles of $\mathscr{H}$ as output from RFM applied to BASE (black line), as well as atmospheric columns with RH = 0.3 (blue line) and $\Gamma = 5$ K/km (red line). **(b)** As in (a), but computed from the SSM1D (15). **(c)** As in (a), but for atmospheres with parameters as in BASE but with varying T_s. **(d)** As in (c), but computed from the SSM1D (15). All RFM profiles are cut-off where the corresponding simple model profile cuts off, for clarity of comparison. The characteristic value of $\mathscr{H}$ does not change significantly with these typical RH and Γ perturbations, but there is a systematic variation with T_s. These effects are exhibited by both RFM and the SSM1D.

and the transmissivity gradient $\partial_p \mathscr{T}_k$. Postponing discussion of $B(k,T)$ for the moment, we begin by plotting $\partial_p \mathscr{T}_k$ for the **rot** band in the upper troposphere for BASE in Fig. 5a. From this plot, however, it is not obvious why $\mathscr{H}$ exhibits a kink at roughly 250 hPa; to the contrary, the characteristic value of $\partial_p \mathscr{T}_k$ actually *increases* with height, in accordance with (7).

Of course, $\mathscr{H}$ involves a spectral integral, so we consider the integrated transmissivity gradient

$$\overline{\partial_p \mathscr{T}_k} \equiv \int_0^{1000\ \mathrm{cm}^{-1}} dk\, \partial_p \mathscr{T}_k \,. \qquad (18)$$

Figure 5b confirms that this quantity does indeed exhibit a kink at the right height, and that this feature is reproduced by the SSM2D. Since transmissivity gradients can also be interpreted as emissivity-to-space gradients (Section 4), this upper-tropospheric kink in $\overline{\partial_p \mathscr{T}_k}$ can also be thought of as a precise quantification of the 'declining water vapor emissivity' referred to in the FAT literature. Also, the kink in $\overline{\partial_p \mathscr{T}_k}$ tells us that additional variations in $B(k,T)$ are not required to produce the kink in $\mathscr{H}_{\mathbf{rot}}$: if $B(k,T)$ were a constant function, $\mathscr{H}_{\mathbf{rot}}$ would be proportional to $\overline{\partial_p \mathscr{T}_k}$ (by the CTS approximation) and hence would also exhibit a kink, without variations in $B(k,T)$.

We may thus conclude that the kink in $\mathscr{H}$ stems from the kink in $\overline{\partial_p \mathscr{T}_k}$. But what, then, causes the kink in $\overline{\partial_p \mathscr{T}_k}$? Since the integrand in (18) is not decreasing with height, a plausible alternative hypothesis is that the kink is due to changes in the spectral range over which $\partial_p \mathscr{T}_k$ is significant, i.e. changes in the effective emitting width Δk. We quantified this earlier in Section 4 as a constant $\Delta k = l_j e$ for the SSM1D, but now generalize it for application to RFM and the SSM2D as simply the range of wavenumbers for which $e^{-e/2} < \tau_k < e^{e/2}$:

$$\Delta k \equiv \int_0^{1000\ \mathrm{cm}^{-1}} dk\, \mathscr{H}(\tau_k - e^{-e/2}) \mathscr{H}(e^{e/2} - \tau_k) \qquad (19)$$

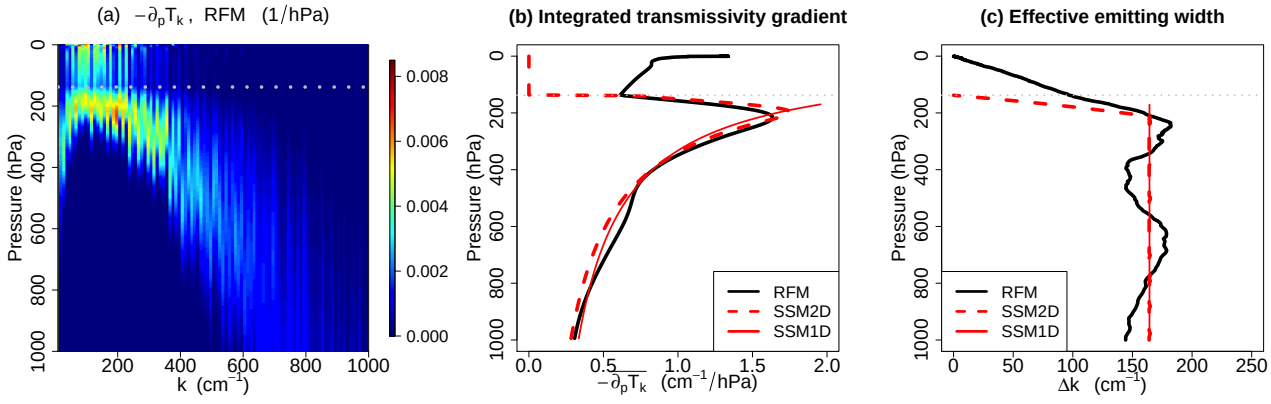

FIG. 5. **(a)** Transmissivity gradient $\partial_p \mathscr{T}_k$ for BASE as computed by RFM, averaged over 10 cm^{-1} bins. **(b)** Spectrally integrated transmissivity gradient $\overline{\partial_p \mathscr{T}_k}$ as defined in (18) for BASE as computed via RFM and the SSM2D. These quantities exhibit upper tropospheric kinks coincident with their kinks in $\mathscr{H}$ (Fig. 3). **(c)** Effective emitting width Δk as computed via (19). Both RFM and the SSM2D exhibit a kink in Δk corresponding to their respective kinks in in panel b). The gray dotted line in all panels is the tropopause, which lies roughly 100 hPa $\sim$ 3.5 km above the RFM kink. All spectral integrations of RFM output are over the **rot** band only, $0 < k < 1000$ cm^{-1}.

Here $\mathscr{H}$ is the Heaviside step function, and the range of τ_k values is chosen such that Δk indeed yields the SSM1D value of $l_{\text{rot}}e \approx 165$ cm^{-1} almost everywhere when calculated for the SSM2D using (10). Profiles of Δk for RFM, the SSM2D and SSM1D are shown in Fig. 5b. Both RFM and SSM2D exhibit a kink in their Δk profiles at the same height at which their respective $\mathscr{H}$ kinks occur. This is consistent with the hypothesis that the kink is caused by a decline in integrated transmissivity gradient $\overline{\partial_p \mathscr{T}_k}$, which itself is caused by a decline in effective emitting width Δk.

What about the kink in Fig. 3 in the SSM1D $\mathscr{H}$ profile? In the SSM1D [Eqn. 16], $\overline{\partial_p \mathscr{T}_k} = \beta_{\text{H}_2\text{O}} l_{\text{rot}}/p$ and $\Delta k = l_{\text{rot}}e$, both of which match the SSM2D in the lower troposphere but neither of which features a kink (Fig. 5b,c, solid red line). According to Eqn. (15), then, the kink in the SSM1D $\mathscr{H}$ profile in Fig. 3 must then stem from an upper-tropospheric decline in $\pi B(k_{1,\text{rot}}, T)$, which as we argued above is not necessary for a kink in the SSM2D or in RFM. This suggests that the SSM1D, by not allowing Δk to vary, is too simple to accurately model the kink in $\mathscr{H}$.

It should also be noted that the agreement in the troposphere between the RFM and SSM2D profiles in Fig. 5b,c benefits to some degree from compensation between the SSM2D's neglect of wavenumbers below $k_{\text{rot}} = 150$ cm^{-1} and its enhancement of bin-averaged $\partial_p \mathscr{T}_k$ (and hence $\mathscr{H}_k$, Fig. 2c,f) due to its neglect of fine-scale structure. These errors do not affect the conclusion, however, that both RFM and the SSM2D exhibit kinks due ultimately to declines in Δk.

7. CO_2

Having addressed questions 1 and 2 from the introduction, we now turn to question 3 concerning the stratospheric enhancement of CO_2 cooling rates. Addressing this question requires applying our formalism to CO_2, which we do now.

For CO_2 cooling we run RFM just as described in Section 2a, except our k range is now 500-850 cm^{-1}, we use a preindustrial CO_2 concentration of 280 ppmv, and RFM's χ factor (from Cousin et al. 1985) is used to suppress far-wing absorption of CO_2. In analogy to (8), we begin by defining bands for CO_2:

$$\begin{aligned} &\text{CO}_2\ P\text{ band:} \quad 500 < k < k_Q \equiv 667.5\ \text{cm}^{-1} \\ &\text{CO}_2\ R\text{ band:} \quad k_Q < k < 850\ \text{cm}^{-1} \end{aligned} \tag{20}$$

(here k_Q denotes the spectral location of the main CO_2 Q branch, which lies between its associated P and R branches but has a much smaller spectral width, e.g. Coakley Jr. and Yang 2014). This band structure can be seen in $\kappa_{\text{ref}}(k)$ as output from RFM, shown in Figure 6a. We then again coarse-grain $\ln \kappa_{\text{ref}}(k)$ over spectral intervals of 10 cm^{-1} and apply a linear fit to $\ln \kappa_{\text{ref}}(k)$ within each band. These linear fits give very similar slopes and maxima, so we combine the two fits into a single expression for simplified reference absorption coefficients

$$\kappa_{\text{CO}_2}(k) \equiv \kappa_Q \exp\left(-\frac{|k-k_Q|}{l_Q}\right) \qquad \text{for } k \text{ in } P \text{ or } R, \tag{21}$$

where $\ln \kappa_Q$ and l_Q are averages of the maxima and slopes from the P and R bands. These parameter values are also tabulated in Table 1. Note that CO_2's l_Q parameter is much

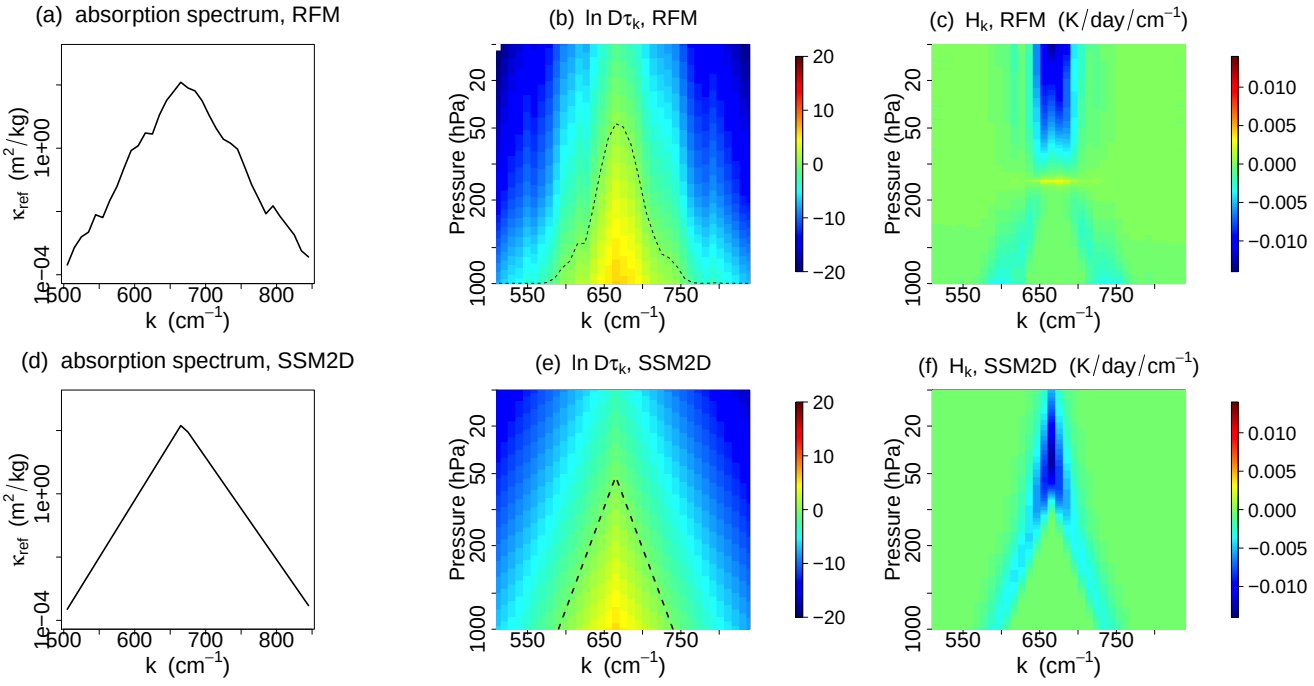

FIG. 6. As for Fig. 2, except for the 500-850 cm^{-1} CO_2 band. The SSM2D emulates the behavior of RFM, and in particular reproduces the stratospheric enhancement of $\mathscr{H}_k$.

smaller than that for H_2O, a point to which we return below.

Next we obtain expressions for CO_2 optical depth. Evaluating (2) with pressure broadening (but no temperature scaling) and constant CO_2 concentration q (rather than variable q_v) yields

$$\tau_k = \kappa_{CO_2}(k)\frac{qp^2}{2gp_{\rm ref}} \,. \tag{22}$$

Note that Eqns. (22) and (5) imply

$$\beta_{CO_2} \;=\; 2 \,,$$

a value 2-3 times smaller than that for H_2O (cf Eqn. (12)).

We can now substitute (22) into (4) to obtain a spectrally simplified $\mathscr{H}_k$. This, along with the expressions (21) for κ_{CO_2} and (22), constitute the SSM2D for CO_2. These fields, along with their RFM counterparts, are shown in Fig. 6. As for H_2O, the SSM2D captures the broad characteristics of the $\mathscr{H}_k$ produced by RFM, though again without fine-scale structure.

In particular, the SSM2D reproduces the stratospheric enhancement of $\mathscr{H}_k$ exhibited by RFM (Fig. 6c,f). From Eqns. (4) and (6) with $\beta_{CO_2} = 2$ we see that this high-altitude enhancement of $\mathscr{H}_k$ stems from the high-altitude enhancement of β/p. But, what is the meaning of this β/p factor? We know that $\beta/p = \frac{d\tau_k}{dp}\Big|_{\tau_k=1}$, but why is this optical depth gradient enhanced at low p? To understand this, note that by (2) we have $\frac{d\tau_k}{dp} = \kappa(k,T,p)q/g$. If we set $\tau_k = 1$ in (22), and solve for the (absolute, not reference) absorption coefficient κ_1 emitting at a given p, we find

$$\kappa_1 \;=\; \frac{2g}{qp}. \tag{23}$$

Thus, at lower pressures this 'effective absorption coefficient' is stronger, and in fact scales as $1/p$. (Note also that substituting (23) into $\kappa q/g$ yields precisely β_{CO_2}/p, as it must.) This $1/p$ scaling is confirmed in Fig. 7, which plots Eqn. (23) as well as κ_1 diagnosed directly from RFM by averaging the absolute absorption coefficients at each height over the same wavenumbers contributing to Δk in Eqn. (19). Physically, $\mathscr{H}_k\,|_{\tau_k=1}$ is enhanced at low p because wavenumbers with such strong κ can cool a unit mass of air at a much higher rate than the more weakly absorbing wavenumbers which reach $\tau_k = 1$ at higher p. This explanation differs from some previously proposed, such as those based on decreased pressure broadening (Petty 2006, pg. 317) or H_2O-CO_2 overlap (Zhu et al. 1992).

We are now also in a position to explain why tropospheric CO_2 cooling rates are negligible compared to H_2O. We noted above that β_{CO_2} is 2-3 times smaller than β_{H_2O}, which by Eqns. (4)-(6) tells us that tropsopheric $\mathscr{H}_k$ will also be 2-3 times smaller for CO_2 (cf. Figs. 2,6). In other words, because CO_2 optical depth does

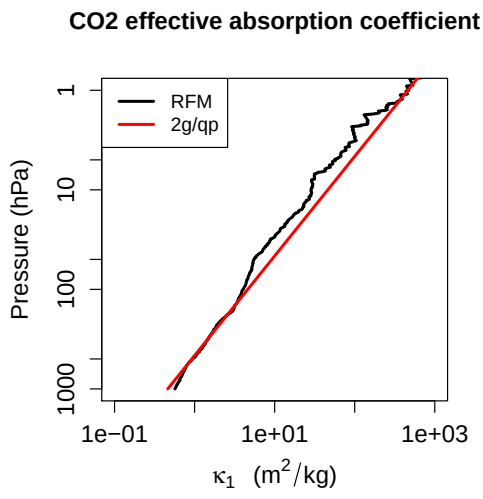

FIG. 7. Profiles of the effective absorption coefficient κ_1 for CO_2, as predicted by (23) (red) as well as diagnosed from RFM (black) by linearly averaging $\kappa(k,p)$ over those k which also contribute to Δk in (19). The good agreement confirms the $1/p$ scaling for κ_1, which underlies the stratospheric enhancement of $\mathscr{H}_k$ (Fig. 6).

not increase with pressure as fast as H_2O, its cooling at any given wavenumber is more spread out in the vertical and is thus smaller. This decrease in $\mathscr{H}_k$ is compounded by CO_2's smaller effective emitting width Δk, which is roughly $l_Q e \approx 35$ cm^{-1}, approximately 1/5 that of H_2O (cf. Figs. 2, 6). Together, these two effects imply that spectrally-integrated radiative cooling $\mathscr{H}$ from CO_2 will only be a fraction of that from H_2O. Due to its relative insignificance in the troposphere, then, we resist the temptation to construct an SSM1D for CO_2, though it is straightforward from here.

8. Summary and discussion

Our main results can be summarized as follows:

- The characteristic $\mathscr{H}$ value of -2 K/day can be obtained as the product of the Planck function, a vertical emissivity gradient, and an effective emitting width, all of which can be estimated via the SSM1D [Eqn. (17)]. This characteristic value is relatively insensitive to typical RH and Γ variations, but is sensitive to T_s (Fig. 4).

- The upper-tropospheric kink in $\mathscr{H}$ is due to a decline in integrated transmissivity gradient $\overline{\partial_p \mathscr{T}_k}$, which is itself caused by a decline in effective emitting width Δk (Fig. 5).

- The stratospheric enhancement of CO_2 cooling is due to the $1/p$ factor in the transmissivity gradient (6). This $1/p$ factor itself can be traced to the strength of the effective absorption coefficients which emit from a given height [Eqn. (23) and Fig. 7].

This work could be generalized and extended in various ways. One extension would be to use the SSM1D, which by providing $\tau_k = 1$ contours identifies an emission height for each wavenumber k, to generate an estimate for spectrally-resolved OLR. A first attempt at this for H_2O only, without the continuum, is given in Appendix B and Fig. B9. Further work could incorporate idealized models of H_2O-CO_2 overlap, as well as the H_2O continuum, for estimation of both $\mathscr{H}$ and OLR. One could also formulate a simplified spectroscopy akin to (9) and (21) for other important greenhouse gases such as methane and ozone, and thus incorporate those gases into the SSMs.

Another direction for future work would be to investigate the radiative cooling profiles of less idealized atmospheres, and in particular atmospheres with non-uniform RH profiles, as non-uniform RH can significantly affect radiative cooling. For example, Seeley et al. (2019) found that the kink disappeared in cloud-resolving radiative-convective equilibrium simulations at T_s of 270 K and colder, but further investigation showed that the kink reappeared when the simulated RH profiles were replaced with a uniform RH profile (not shown). Observations of non-uniform RH profiles are discussed in Stevens et al. (2017), who focused on strong vertical RH gradients observed in the subtropics and emphasized the implications of these RH gradients for radiative cooling profiles and the associated circulations. Similar effects have also been studied in the context of radiative instabilities and self-aggregation of convection (Beucler et al. 2018; Beucler and Cronin 2016; Emanuel et al. 2014). Extending the present work to include non-uniform RH might allow for greater understanding and ease of modeling of phenomena such as these.

While the primary goal of this work was to shed light on questions 1-3 posed in the introduction, an ancillary benefit was the development of the SSMs, which might be thought of as filling in the intermediate rungs of a 'radiation hierarchy', with gray models on the bottom rung and line-by-line codes like RFM at the top. Moving between these rungs to generate and test hypotheses exemplifies the 'hierarchical' approach to climate science, which has been much discussed recently but also goes back decades (Maher et al. 2019; Jeevanjee et al. 2017; Polvani et al. 2017; Held 2005; Hoskins 1983; Schneider and Dickinson 1974).

Another use of these simple models is to make back-of-the-envelope calculations, as we did in Section 4b. Another example is as follows. The maximum value κ_{rot}

of κ_{H_2O} in the **rot** band (cf. Eqn. (9)) can be inverted to yield the minimum water vapor path WVP_{min} required to 'activate' the **rot** band, in the sense of creating a swath of wavenumbers of width $\Delta k = l_{rot}e$ which are cooling to space. Setting $\kappa_{H_2O} = \kappa_{rot}$ and $p = 100$ hPa in (10) and solving for this water vapor path yields $WVP_{min} = 0.04$ kg/m^2. This can be compared with a stratospheric water vapor path of 0.005 kg/m^2 (assuming a stratospheric mass of 2000 kg/m^2 and a specific humidity of 4 ppmv). This suggests that stratospheric H_2O cooling is in a different regime wherein cooling is only occurring from narrower spectral regions near line centers, as indeed suggested by Fig. 5c and evident in Fig. 2c.

The intermediate complexity SSMs could also be used to augment or replace gray models where they are still used for research purposes, as the distortions of the gray approximation evident in Fig. 1b suggest that inferences drawn from gray radiation models, as well as fluid-dynamical models coupled to them, may not be reliable (e.g. Tan et al. 2019).[8] Gray models are in use in both astronomy (e.g. Parmentier and Guillot 2014; Rauscher and Menou 2012; Robinson and Catling 2012; Heng et al. 2011) as well as terrestrial atmospheric sciences, particularly as radiation schemes for idealized aquaplanet models [e.g. Vallis et al. (2015); Frierson et al. (2006); see Maher et al. (2019) and Jeevanjee et al. (2017) for further references to gray radiation aquaplanet studies]. The SSMs could prove useful as alternative, cheap, clear-sky radiation schemes which still only depend on a few parameters (cf. Table 1) but are nonetheless spectral and avoid the distortions of the gray approximation.

Acknowledgments. We thank ECMWF for providing the ERA Interim data. This research was supported by NSF grants AGS-1417659 and AGS-1660538, and NJ was supported by a Hess fellowship from the Princeton Geosciences department. NJ thanks David Romps for guidance in early stages of this work and for suggesting the delta function approach to integrating Eqn. (14). NJ also thanks Jacob Seeley and Robert Pincus for discussions, feedback, and encouragement, as well as three anonymous reviewers for helpful and detailed reviews. RFM output and R scripts used in producing this manuscript are available at https://github.com/jeevanje/17rad_cooling2.git.

APPENDIX A

Sensitivity to H_2O continuum and CO_2 overlap

The RFM calculations in the main text neglected the water vapor continuum as well as overlap effects between H_2O and CO_2, both of which are known to affect radiative cooling and OLR. While we do not pursue simple models of these effects, this appendix investigates the errors induced by neglecting them, and discusses why our 1D RFM calculation which neglects these effects nonetheless resembles the ECMWF profile in Fig. 1b, which includes them.

We first consider the H_2O continuum. Figure A8a shows $\mathscr{H}_k$ from an RFM calculation identical to BASE, but with the continuum turned on (RFM contains a hard-coded version of the MT_CKD continuum, Mlawer et al. 2012). The spectrally integrated $\mathscr{H}$ profile from this case is shown in Fig. A8c. The continuum increases $\mathscr{H}$ throughout the troposphere, especially at lower levels. When we then add on the effects of CO_2 overlap (Fig. A8b,c), however, we find that much of this increase is cancelled due to the presence of CO_2. From Fig. A8c we see that the only real contrast between our base case and the more realistic case with both continuum and CO_2 contributions is for pressures greater than 850 hPa or so, corresponding to temperatures of 290 or above (thinking here in temperature coordinates). Such temperatures may not necessarily make a strong contribution to the globally averaged $\mathscr{H}$ profile shown in Fig. 1, which is averaged on pressure levels and thus conflates different temperatures.

APPENDIX B

OLR

The formalism developed here can also be applied to estimate the spectrally resolved outgoing longwave radiation $OLR_k \equiv F_k(p = 0)$, where we estimate this as simply the Planck function evaluated at an effective emission temperature $T_1(k)$. We estimate this by setting $\tau_k = 1$ in (10) and solving for T, where we first substitute in

$$p \;=\; p_s \left(\frac{T}{T_s}\right)^{g/R_d\Gamma}$$

for p. This yields a transcendental equation for T which can nonetheless be solved using the Lambert W-function, which satisfies $W(xe^x) = x$, i.e. it inverts the function xe^x. After some algebraic manipulation of Eqn. (10) to put it into the form xe^x, we obtain

$$T_1(k) \;=\; \frac{T^*}{W\left(\frac{T^*}{T_s}\tau_0^{R_d\Gamma/g}\right)}$$

where

$$T^* \;\equiv\; \frac{R_d\Gamma L}{gR_v}\,, \qquad \tau_0(k) \;\equiv\; \mathrm{WVP}_0\,\kappa(k)\frac{p_s}{p_{\mathrm{ref}}}\,.$$

For some k, however, $T_1(k)$ will be undefined because $\tau_k < 1$ even at the surface; this is the water vapor 'window' region $k_{rot}(T_s) < k < k_{v\text{-}r}(T_s)$, for which we set OLR_k equal

[8] Also note that the gray model in Fig. 1b, tuned to exhibit the same 170 W/m^2 column-integrated cooling as RFM, also yields an OLR of 170 W/m^2. This is a serious underestimate of RFM's OLR value of 325 W/m^2.

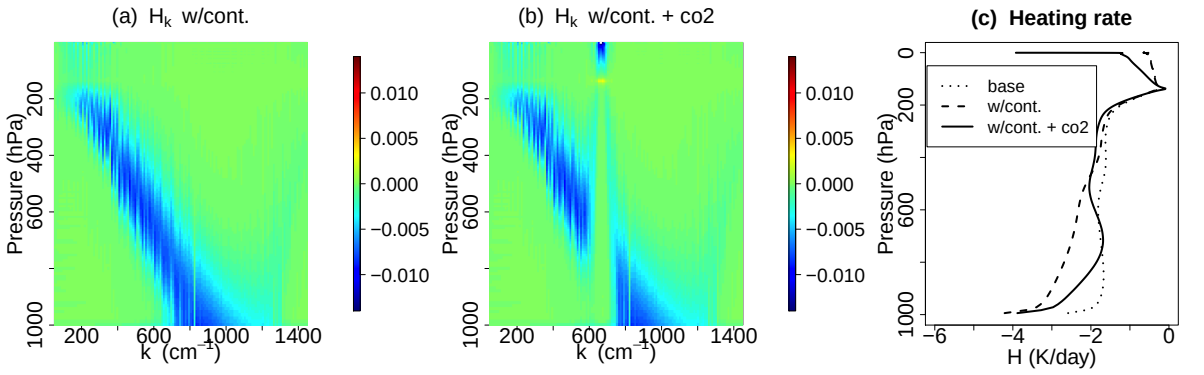

FIG. A8. Spectrally resolved radiative cooling $\mathscr{H}_k$ as output from RFM for the BASE atmosphere with **(a)** the H_2O continuum included and **(b)** H_2O continuum plus CO_2 absorption. Panel **(c)** shows the spectrally integrated cooling rates $\mathscr{H}$ for these cases plus BASE. Continuum emission enhances $\mathscr{H}$, particularly in the lower troposphere, but this effect is largely canceled out by CO_2 absorption.

to surface Planck emission. Mathematically, our estimate for OLR_k is then

$$\mathrm{OLR}_k = \begin{cases} \pi B(k, T_1(k)) & \text{where } T_1(k) \text{ is defined} \\ \pi B(k, T_s) & \text{where } k_{\mathrm{rot}}(T_s) < k < k_{\text{v-r}}(T_s) \end{cases} . \quad \text{(B1)}$$

Figure B9 shows this estimate of OLR_k, along with OLR_k as output directly from RFM. The estimate (B1), while crude, quantitatively captures the gross spectral shape of RFM's OLR_k. Furthermore, it gives us some insight into this shape, as follows. Both the RFM and simple model OLR_k curves peak at the beginning of the window region, $k_{\mathrm{rot}}(T_s) \approx 750\ \mathrm{cm}^{-1}$, and the simple OLR_k estimate in particular has a cusp. This is because beyond $k_{\mathrm{rot}}(T_s)$, the emission temperature is no longer increasing with k but rather becomes constant at T_s, allowing the explicit k-dependence of $B(k,T)$ to take over and cause an immediate and sharp decline in OLR_k. Thus the peak in OLR_k is caused by a temperature driven increase for $k < k_{\mathrm{rot}}(T_s)$ and a k-driven decrease for $k > k_{\mathrm{rot}}(T_s)$. Adding the H_2O continuum to our RFM calculation does not change this picture (Fig. B9, dotted line). This peak is typically obscured in more realistic calculations by the strong 667 cm^{-1} CO_2 absorption feature, but understanding the H_2O-only case seems like a prerequisite for understanding these more realistic cases, which could be pursued along similar lines.

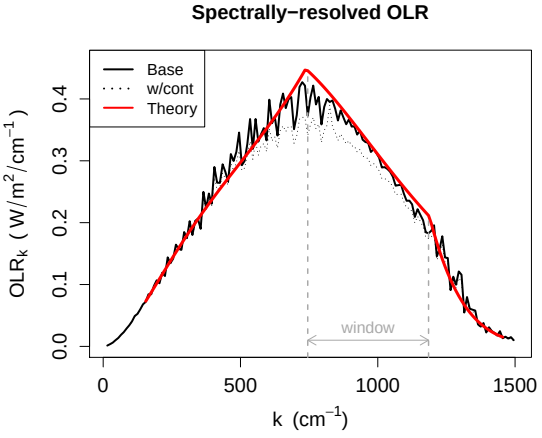

FIG. B9. Spectrally resolved outgoing longwave radiation OLR_k, as computed from RFM (black line) and Eqn. (B1) (red line). Equation (B1) captures the shape of RFM's OLR_k, and also shows that the peak in OLR_k is due to the onset of the water vapor window. This conclusion is unchanged by comparing to RFM's OLR_k computed with the H_2O continuum (dotted line).

References

Beucler, T., T. Cronin, and K. Emanuel, 2018: A Linear Response Framework for Radiative-Convective Instability. *Journal of Advances in Modeling Earth Systems*, **10 (8)**, 1924–1951.

Beucler, T., and T. W. Cronin, 2016: Moisture-radiative cooling instability. *Journal of Advances in Modeling Earth Systems*, 1–39.

Clough, S. A., M. J. Iacono, and J.-l. Moncet, 1992: Line-by-line calculations of atmospheric fluxes and cooling rates: Application to water vapor. *Journal of Geophysical Research*, **97 (D14)**, 15 761.

Coakley Jr., J. A., and P. Yang, 2014: *Atmospheric Radiation: A Primer with Illustrative Solutions*. Wiley-VCH, 239 pp.

Costa, S. M. S., and K. P. Shine, 2012: Outgoing Longwave Radiation due to Directly Transmitted Surface Emission. *Journal of the Atmospheric Sciences*, **69 (6)**, 1865–1870.

Cousin, C., R. L. Doucen, C. Boulet, and a. Henry, 1985: Temperature dependence of the absorption in the region beyond the 4.3-microm band head of CO(2) . 2: N(2) and O(2) broadening. *Applied optics*, **24 (22)**, 3899–3907.

Dudhia, A., 2017: The Reference Forward Model (RFM). *Journal of Quantitative Spectroscopy and Radiative Transfer*, **186**, 243–253.

Emanuel, K. A., A. A. Wing, and E. M. Vincent, 2014: Radiative-convective instability. *Journal of Advances in Modeling Earth Systems*, **6 (1)**, 75–90.

Frierson, D. M. W., I. M. Held, and P. Zurita-Gotor, 2006: A Gray-Radiation Aquaplanet Moist GCM. Part I: Static Stability and Eddy Scale. *Journal of the Atmospheric Sciences*, **63 (10)**, 2548–2566.

Gasiorowicz, S., 2003: *Quantum physics*. Wiley, 336 pp.

Green, J. S., 1967: Division of radiative streams into internal transfer and cooling to space. *Quarterly Journal of the Royal Meteorological Society*, **93 (397)**, 371–372.

Harries, J., and Coauthors, 2008: the Far-Infrared Earth. *Reviews of Geophysics*, **46**, 1–34.

Hartmann, D. L., J. R. Holton, and Q. Fu, 2001: The heat balance of the tropical tropopause, cirrus, and stratospheric dehydration. *Geophysical Research Letters*, **28 (10)**, 1969–1972.

Hartmann, D. L., and K. Larson, 2002: An important constraint on tropical cloud - climate feedback. *Geophysical Research Letters*, **29 (20)**, 1951.

Held, I. M., 2005: The gap between simulation and understanding in climate modeling. *Bulletin of the American Meteorological Society*, **86 (11)**, 1609–1614.

Heng, K., D. M. W. Frierson, and P. J. Phillipps, 2011: Atmospheric circulation of tidally locked exoplanets: II. Dual-band radiative transfer and convective adjustment. *Monthly Notices of the Royal Astronomical Society*, **418 (4)**, 2669–2696.

Hoskins, B. J., 1983: Dynamical processes in the atmosphere and the use of models. *Quart. J. R. Met. SOC*, **109 (459)**, 313.

Jeevanjee, N., and S. Fueglistaler, 2019: On the cooling-to-space approximation. *Submitted to Journal of Atmospheric Sciences*.

Jeevanjee, N., P. Hassanzadeh, S. Hill, and A. Sheshadri, 2017: A perspective on climate model hierarchies. *Journal of Advances in Modeling Earth Systems*, **9 (4)**, 1760–1771.

Koll, D. D. B., and T. W. Cronin, 2018: Earth's outgoing longwave radiation linear due to H 2 O greenhouse effect. *Proceedings of the National Academy of Sciences*, 201809868.

Maher, P., and Coauthors, 2019: The value of hierarchies and simple models in atmospheric. *Math.Nyu.Edu*.

Manabe, S., R. F. Strickler, S. Manabe, and R. F. Strickler, 1964: Thermal Equilibrium of the Atmosphere with a Convective Adjustment. *Journal of the Atmospheric Sciences*, **21 (4)**, 361–385.

Mapes, B. E., 2001: Water's Two Scale Heights: The Moist Adiabat and the Radiative Troposphere. *Quarterly Journal of the Royal Meteorological Society*, **127 (January)**, 2353–2366.

Mlawer, E. J., V. H. Payne, J.-L. Moncet, J. S. Delamere, M. J. Alvarado, and D. C. Tobin, 2012: Development and recent evaluation of the MT_CKD model of continuum absorption. *Philosophical Transactions of the Royal Society A: Mathematical, Physical and Engineering Sciences*, **370 (1968)**, 2520–2556.

Parmentier, V., and T. Guillot, 2014: A non-grey analytical model for irradiated atmospheres. I. Derivation. *Astronomy & Astrophysics*, **562**, 133, arXiv:1311.6597v1.

Petty, G. W., 2006: *A First Course in Atmospheric Radiation (2nd Ed.)*. Sundog Pub, 472 pp.

Pierrehumbert, R. T., 2010: *Principles of Planetary Climate*. Cambridge University Press, Cambridge, UK.

Polvani, L., B. Medeiros, I. Simpson, A. Clement, and J. Benedict, 2017: When Less Is More: Opening the Door to Simpler Climate Models. *Eos*, **98 (September)**.

Rauscher, E., and K. Menou, 2012: A GENERAL CIRCULATION MODEL FOR GASEOUS EXOPLANETS WITH DOUBLE-GRAY RADIATIVE TRANSFER. *The Astrophysical Journal*, **750 (2)**, 96.

Robinson, T. D., and D. C. Catling, 2012: An analytic radiative-convective model For planetary atmospheres. *The Astrophysical Journal*, **757 (1)**, 104.

Rodgers, C. D., and C. D. Walshaw, 1966: The computation of infrared cooling rate in planetary atmospheres. *Quarterly Journal of the Royal Meteorological Society*, **92**, 67–92.

Schneider, S. H., and R. E. Dickinson, 1974: Climate modeling. *Reviews of Geophysics*, **12 (3)**, 447.

Seeley, J. T., N. Jeevanjee, and D. M. Romps, 2019: FAT or FiTT: Are anvil clouds or the tropopause temperature-invariant? *Geophysical Research Letters*, **46 (3)**, 1842–1850.

Shine, K. P., I. V. Ptashnik, and G. Rädel, 2012: The Water Vapour Continuum: Brief History and Recent Developments. *Surveys in Geophysics*, **33 (3-4)**, 535–555.

Stevens, B., H. Brogniez, C. Kiemle, J. L. Lacour, C. Crevoisier, and J. Kiliani, 2017: Structure and Dynamical Influence of Water Vapor in the Lower Tropical Troposphere. *Surveys in Geophysics*, **38 (6)**, 1371–1397.

Tan, Z., O. Lachmy, and T. A. Shaw, 2019: The sensitivity of the jet stream response to climate change to radiative assumptions. *Journal of Advances in Modeling Earth Systems*, 2018MS001492.

Thompson, D. W. J., S. Bony, and Y. Li, 2017: Thermodynamic constraint on the depth of the global tropospheric circulation. *Proceedings of the National Academy of Sciences*, **114 (31)**, 8181–8186, arXiv:1408.1149.

Vallis, G. K., P. Zurita-Gotor, C. Cairns, and J. Kidston, 2015: Response of the large-scale structure of the atmosphere to global warming. *Quarterly Journal of the Royal Meteorological Society*, **141 (690)**, 1479–1501.

Wallace, J. M., and P. V. Hobbs, 2006: *Atmospheric Science: An Introductory Survey*. Academic Press, 504 pp.

Wilson, D. J., and J. Gea-Banacloche, 2012: Simple model to estimate the contribution of atmospheric CO2 to the Earth's greenhouse effect. *American Journal of Physics*, **80 (4)**, 306.

Zhu, X., M. E. Summers, and D. F. Strobel, 1992: Calculation of CO ₂ 15-μm band atmospheric cooling rates by Curtis matrix interpolation of correlated- k coefficients. *Journal of Geophysical Research*, **97 (D12)**, 12 787.